Advances in Geo-Energy Research

Vol. 21, No. 3, p. 205-219, 2026

Original article

Nanoscale confinement effects of pore radius and mineral type on shale oil component diffusion in porous media

Changran Lv[1,2], Yongfei Yang[1,2]*, Qi Zhang[1,2], Yingwen Li[1], Vadim Lisitsa[3], Jun Yao[1,2]

[1]*State Key Laboratory of Deep Oil and Gas, China University of Petroleum (East China), Qingdao 266580, P. R. China*

[2]*Center of Multiphase Flow in Porous Media, School of Petroleum Engineering, China University of Petroleum (East China), Qingdao 266580, P. R. China*

[3]*Institute of Petroleum Geology and Geophysics SB RAS, Novosibirsk 630090, Russia*

Keywords:
Shale oil
nanoscale confinement effects
diffusion
porous media

Cited as:
Lv, C., Yang, Y., Zhang, Q., Li, Y., Lisitsa, V., Yao, J. Nanoscale confinement effects of pore radius and mineral type on shale oil component diffusion in porous media. Advances in Geo-Energy Research, 2026, 21(3): 205-219.
https://doi.org/10.46690/ager.2026.09.02

Abstract:
Shale oil plays an increasingly prominent role in compensating for the depletion of conventional hydrocarbon resources. While nanoscale confinement in shale nanopores can substantially alter hydrocarbon diffusivity, pore-scale models capable of explicitly incorporating the combined effects of pore size and pore-wall properties remain limited. In this study, molecular dynamics simulations of n-octane confined in quartz and kerogen nanopores were conducted to establish pore-radius-dependent diffusion relationships for inorganic and organic pores. These relationships were incorporated into a modified OpenFOAM species-transport solver, enabling the local diffusion coefficient to vary according to the pore radius and the pore type. Multi-mineral shale porous structures were reconstructed using the Voronoi method combined with a stochastic algorithm, and pore-scale simulations were performed to investigate the effects of heterogeneous diffusivity, pore radius and total organic carbon content on matrix-fracture component transport. The results showed that nanoscale confinement suppresses n-octane transport from the nanoporous matrix to the fracture and increases spatial heterogeneity in component distribution. A decreasing pore radius reduces the overall diffusion capacity, while an increasing organic matter content increases the proportion of low-diffusivity organic pores and enhances component retention within the matrix. These findings demonstrate that spatial variations in molecular diffusivity should be explicitly considered when describing shale oil component transport. The proposed framework provides a practical bridge between molecular-scale confined diffusion and pore-scale transport modeling in heterogeneous shale porous media.

1. Introduction

At present, with the gradual depletion of conventional oil and gas resources, unconventional hydrocarbon resources such as shale oil and gas have become increasingly important in ensuring global energy supply (Xu et al., 2022b; Fu and He, 2024; Wang et al., 2025b). Shale reservoirs are characterized by low porosity, ultra-low permeability, multiscale pore systems, and diverse mineral compositions (Xiang et al., 2024; Luo et al., 2025; Sang et al., 2026). Pore sizes in shale reservoirs are mainly distributed at the nanoscale, with the presence of organic kerogen further complicating the occurrence state of oil and gas within the reservoir (Ji et al., 2019; Xu et al., 2022a). Under such nanoscale confinement, fluid-wall interactions may induce adsorption/desorption, surface diffusion and slip-related effects, thereby modifying the transport behavior of hydrocarbons relative to that in conventional porous media (Yang et al., 2023). Meanwhile, the phenomenon of "component flow" has been observed during the production of

Yandy Scientific Press

*Corresponding author.
E-mail address: s24020012@s.upc.edu.cn (C. Lv); yangyongfei@upc.edu.cn (Y. Yang); b21020012@s.upc.edu.cn (Q. Zhang); b20020034@s.upc.edu.cn (Y. Li); lisitsavv@ipgg.sbras.ru (V. Lisitsa); rcogfr_upc@126.com (J. Yao).
2207-9963 © The Author(s) 2026.
Received June 22, 2026; revised July 23, 2026; accepted August 2, 2026; available online August 5, 2026.

some shale oil reservoirs, where different components of shale oil are produced in different sequences (Zhao et al., 2026). This component-dependent production behavior suggests that shale oil recovery is controlled not only by the bulk motion of the fluid but also by component-specific transport processes associated with the nanoscale pore environment.

In shale reservoirs, an important process governing shale oil recovery is the transfer of hydrocarbon components from the nanoporous matrix to conductive fractures. Species transport in porous media occurs through two distinct mechanisms: Advection and molecular diffusion. Advection is associated with bulk fluid motion, whereas molecular diffusion results from component migration driven by concentration or chemical-potential gradients. In the shale matrix, pressure-driven fluid velocities are strongly restricted by the ultra-low permeability and tortuous nanoporous structure, whereas substantial concentration gradients may develop between the matrix and fractures during production. The relative importance of advective and diffusive transport can be characterized by the Péclet number (Huysmans and Dassargues, 2005):

$$\mathrm{Pe} = \frac{UL}{D} \tag{1}$$

where Pe, U, L and D denote the Péclet number, characteristic fluid velocity, transport length and molecular diffusion coefficient, respectively. For the low-velocity matrix transport conditions considered in the present study, the characteristic Pe is much smaller than unity. This indicates a diffusion-dominated transport regime within the nanoporous matrix (Huysmans and Dassargues, 2005; Tran et al., 2021; Liu et al., 2025). Therefore, molecular diffusion plays a particularly important role in controlling the transfer of shale oil components from the matrix toward the fracture. Accordingly, molecular diffusivity becomes a key parameter controlling matrix-fracture component transfer.

Molecular dynamics (MD) simulations have been applied extensively to investigate the microscopic transport and interfacial behavior of shale oil and related fluids in nanoporous media (Cai et al., 2024a, 2024b; Wang et al., 2025b). At the nanoscale, diffusivity is strongly influenced by the local pore environment (Xu et al., 2024; Zhang et al., 2024; Jia et al., 2026). Numerous molecular dynamics studies have demonstrated that confined hydrocarbon transport is affected by pore size (Wang et al., 2016), pore wall composition and mineral type (Wang et al., 2018; Fei et al., 2023), water-related interfacial effects (Bao et al., 2025), as well as fluid-wall interactions and adsorption (Xue et al., 2022). In addition, temperature and pressure can substantially influence molecular diffusion under confinement (Zhong et al., 2025). Beyond these thermodynamic effects, pore size represents another important factor controlling confined transport. Previous studies have shown that the diffusion coefficient of shale oil in organic nanopores decreases continuously with decreasing pore radius, while the formation of a central water film further reduces molecular diffusivity (Zhang et al., 2025b). However, pore size alone cannot fully characterize the confinement effect, because the physicochemical properties of pore walls also govern molecular mobility. Molecular dynamics simulations of methane, propane and n-octane in graphene and quartz nanopores have revealed that adsorption layers near slit-pore walls reduce molecular mobility and self-diffusion coefficients, with the extent of suppression depending on wall wettability (Dong et al., 2022; Cui et al., 2022). Differences in pore-wall composition further lead to distinct transport behaviors among different minerals. In particular, shale oil exhibits significantly higher diffusivity in graphene slits than in quartz and montmorillonite slits, mainly because the ultrasmooth graphene surface produces weaker fluid-wall interactions (Zhang et al., 2019). This difference also raises an important issue regarding how organic nanopore surfaces are represented in molecular models. Realistic kerogen models incorporating surface heterogeneity and heteroatom distributions predict significantly lower fluid transport rates than simplified graphene-based organic pore models. This reduction is mainly attributed to stronger adsorption layers near kerogen surfaces, which restrict molecular mobility and retard shale oil diffusion and flow (Wang et al., 2022). The molecular representation of organic matter is therefore critical for describing transport in shale nanopores, and realistic molecular models have been developed to capture the heterogeneous nanostructure of kerogen (Bousige et al., 2016). Consistently, comparisons between simplified carbon-based nanopores, such as graphene and carbon nanotubes, and realistic kerogen pores further indicate that representing organic pore walls using extremely smooth graphene surfaces may introduce errors of several orders of magnitude in the predicted fluxes (Zhan et al., 2024).

Collectively, the above molecular-scale studies have demonstrated that nanoscale confinement substantially modifies hydrocarbon diffusivity and that pore size and pore-wall properties are two key controlling factors, providing a molecular-scale basis for treating diffusivity as a pore-dependent quantity rather than a spatially uniform constant. In fact, molecular dynamics simulations have greatly advanced the understanding of confined diffusion mechanisms, and molecular-scale transport information has increasingly been incorporated into pore-scale numerical models. Among these methods, the lattice Boltzmann method and pore network modeling have been widely employed to investigate the flow and diffusion behavior of shale oil components (Zhao et al., 2018; Yang et al., 2019; Duan et al., 2022; Lv et al., 2026). Molecular-scale information has been incorporated into lattice Boltzmann simulations by relating molecular interaction forces to diffusion coefficients and Péclet numbers, enabling the simulation of competitive adsorption and miscible diffusion between CO_2 and shale oil (Wang et al., 2025a). Nanoscale organic-pore gas-flow models have also been developed to account for transport mechanisms and occurrence states, showing that gas occurrence state, pore geometry and pore size all strongly affect transport behavior, with relatively weak adsorbed-phase surface diffusion in elongated pores (Song et al., 2021). In addition, molecular dynamics results have been coupled with pore network models by establishing relationships between confined and bulk CO_2 diffusivities and incorporating them into convection-diffusion equations to simulate diffusive mass transfer between CO_2 and shale oil (Feng et al., 2024). Despite these advances, the high computational

cost of molecular dynamics simulations generally restricts their application to simplified or individual nanopores, whereas pore-scale models often represent molecular diffusivity using a spatially uniform value or simplified effective parameter. Consequently, a scale-bridging gap remains because the spatial heterogeneity in diffusivity arising simultaneously from local pore size and pore-wall properties is not explicitly retained in many pore-scale simulations (Song et al., 2024).

To bridge this molecular-to-pore-scale gap, this study first generated nanoporous multi-mineral shale structures using the Voronoi method combined with a stochastic reconstruction algorithm. Independent molecular dynamics simulations were used to establish pore-radius-dependent diffusion relationships for representative inorganic and organic nanopores. A pore-based diffusion coefficient model was then developed to map these molecular-scale relationships onto the pore-scale computational domain according to the local pore radius and the pore type. Pore-resolved simulations were subsequently performed by solving the fluid-flow field together with the species advection-diffusion equation, in which advection is governed by the local velocity field and molecular diffusion is driven by the spatially varying pore-based diffusivity. The Péclet number was further evaluated to identify the dominant transport mechanism. Finally, the effects of heterogeneous diffusivity, pore radius and total organic carbon (TOC) content on matrix-fracture component transport and retention were systematically investigated. This framework provides a direct molecular-to-pore-scale route for representing nanoscale confinement effects in structurally and mineralogically heterogeneous shale porous media.

2. Materials and methodology

2.1 Construction of multi-mineral nanoporous shale media

In this study, nanoporous media with controllable pore structures were constructed using a porous-medium generation method based on the Centroidal Voronoi Tessellation. The Voronoi method is a geometric partitioning approach based on the nearest-neighbor principle, in which the computational domain is divided into a set of non-overlapping subregions according to the shortest-distance relationship between any spatial location and a group of seed points, with each subregion corresponding to the zone of influence of one seed point (Voronoi, 1908). In recent years, this method has been widely applied in digital rock and porous-media generation, microfluidic chip design, and clay particle analysis, and has achieved substantial research progress. It has also been demonstrated that the Voronoi method is well suited for constructing porous-media structures (Wu et al., 2012; Xiao and Yin, 2016; Zhang et al., 2021). On this basis, thus paper used the Centroidal Voronoi Tessellation method to generate the nanoporous medium, with the basic procedure described as follows.

First, a set of random seed points $P = \{p_i\}_{i=1}^{N}$ was generated within the computational domain $\Omega = \mathbb{R}^2$, and the space was partitioned into a series of grain units through Voronoi tessellation, expressed as (Voronoi, 1908; Du et al., 1999):

$$V_i = \left\{x \in \Omega | d(x, p_i) \le d(x, p_j), \forall j \ne i\right\} \tag{2}$$

where $d(\cdot)$ denotes the Euclidean distance function; V_i represents the i^{th} Voronoi cell; p_i denotes the i^{th} seed point; p_j denotes the j^{th} seed point; and x is an arbitrary spatial point (e.g., a pixel or grid point). To obtain a more uniform grain structure, Lloyd iteration was employed to update the seed point of each Voronoi cell to its centroid, thereby forming a centroidal Voronoi tessellation structure, expressed as:

$$p_i^{k+1} = \frac{\int_{V_i} x \mathrm{d}x}{\int_{V_i} \mathrm{d}x} \tag{3}$$

where p_i^{k+1} denotes the position of the i^{th} seed point after the $(k+1)^{\text{th}}$ Lloyd iteration.

The pore space of the porous medium was constructed from the boundaries between Voronoi cells, where $L(x)$ denotes the label field. Then, the boundary set could be defined as shown in Eq. (4). Furthermore, the minimum distance from an arbitrary spatial point to the boundary set was calculated using Eq. (5) to characterize its positional relationship with respect to the pore boundary (Maurer et al., 2003):

$$B(x) = \{x | L(x) \ne L(x+\sigma)\} \tag{4}$$

$$D(x) = \min_{y \in B} ||x - y|| \tag{5}$$

where $B(x)$ denotes the set of boundary points; σ is a small perturbation vector; $D(x)$ represents the shortest Euclidean distance from the spatial point x to the boundary set $B(x)$, y denotes an arbitrary boundary point belonging to $B(x)$.

To achieve controllable construction of the pore structure, a pore-throat control parameter t and a target porosity ϕ_t were introduced. Eqs. (6), (7) and (8) were then used to regulate the porosity and the pore radius, thereby constructing nanoporous media with similar porosities but different pore-radius distributions:

$$P(t) = \{x | D(x) \le t\} \tag{6}$$

$$\phi_t \frac{|P(t)|}{|\Omega|} \tag{7}$$

$$|\phi(t) - \phi_t| < \varepsilon \tag{8}$$

where $P(t)$ denotes the pore-space set corresponding to the threshold t; $\phi(t)$ represents the porosity under the threshold; and ε is a sufficiently small positive number.

On the basis of the above method, three T-shaped nanoporous media models were constructed to represent the interfacial region between nanoporous media and microfractures in subsurface shale reservoirs. Each model consisted of a regular fracture with identical dimensions and an adjacent porous-medium region. Subsequently, the pore-structure parameters of the porous-medium region, including porosity, pore equivalent radius, and pore coordination number, were extracted and characterized using the Interactive Thresholding, Separate Objects, and Generate Pore Network Model functions in Avizo (Zhang et al., 2025a). In the pore-network extraction, each irregular pore body was represented by an equivalent sphere having the same pore volume. Accordingly, the equivalent pore radius of pore i was calculated as:

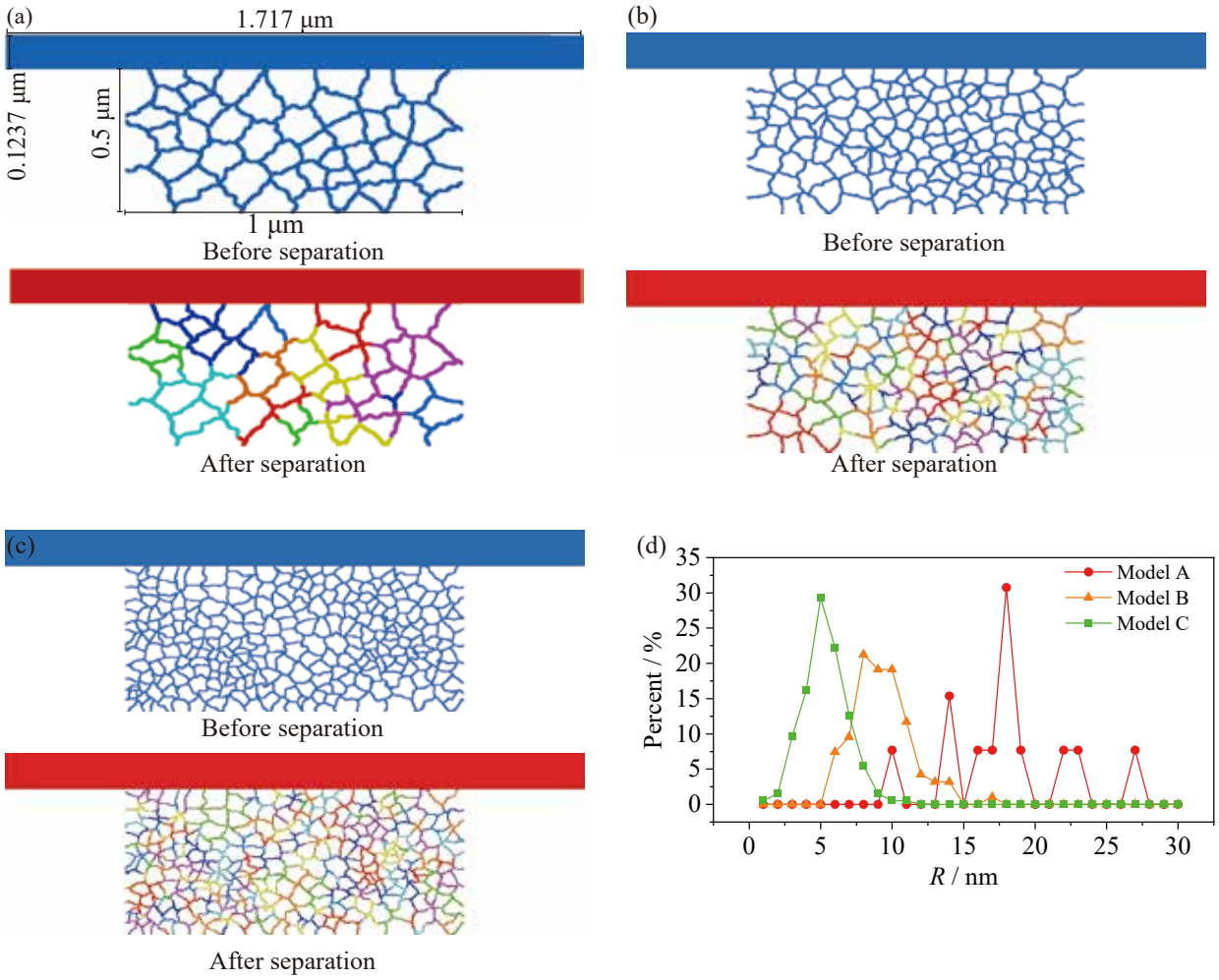


Fig. 1. Porous media model and its pore parameter distribution: (a) Model A, (b) model B, (c) model C and (d) distribution of pore radii. In the segmented images, each colored region represents an individual pore identified after pore segmentation.

Table 1. Pore parameters of the porous media model.

Model	Porosity (%)	Average equivalent pore radius (nm)	Average coordination number (-)
A	24.83	18.07	2.84
B	25.62	9.33	3.93
C	24.79	7.35	3.87

$$R_{eq,i} = \left(\frac{3V_{p,i}}{4\pi}\right)^{1/3} \tag{9}$$

where $V_{p,i}$ represents the volume of pore i, and $R_{eq,i}$ is its equivalent pore radius. The average equivalent pore radius of the porous medium was then calculated as:

$$R_a = N^{-1}\sum_{i=1}^{N} R_{eq,i} \tag{10}$$

where R_a denotes the average equivalent pore radius and N is the total number of identified pores. As shown in Table 1, Models A, B and C were designed to have similar porosities (24.83%, 25.62% and 24.79%, respectively), while their average equivalent pore radii were 18.07 nm, 9.33 nm and 7.35 nm, respectively. These models provide porous structures with comparable porosities but systematically different characteristic pore sizes for evaluating the influence of pore size on component transport. Fig. 1 presents the pore structures of the three models together with the distributions of equivalent pore radii. In contrast, the peak of the equivalent pore radius distribution shifts noticeably from Model A to Model C, reflecting the systematic variation in pore size. Combined with the data summarized in Table 1, these results demonstrate that the three models possess nearly identical porosities and similar pore connectivity, while they exhibit distinctly different average equivalent pore radii.

The mineral constituents in shale nanoporous media have a significant influence on fluid flow and diffusion. This is because organic matter and inorganic minerals exhibit distinct surface physicochemical properties, leading to different fluid-wall interactions under nanoscale confinement. Therefore, the constructed porous-medium models should incorporate multiple mineral constituents to better represent the mineralogical heterogeneity of shale reservoirs and provide a basis for investigating the effects of mineral types on the fluid transport be-

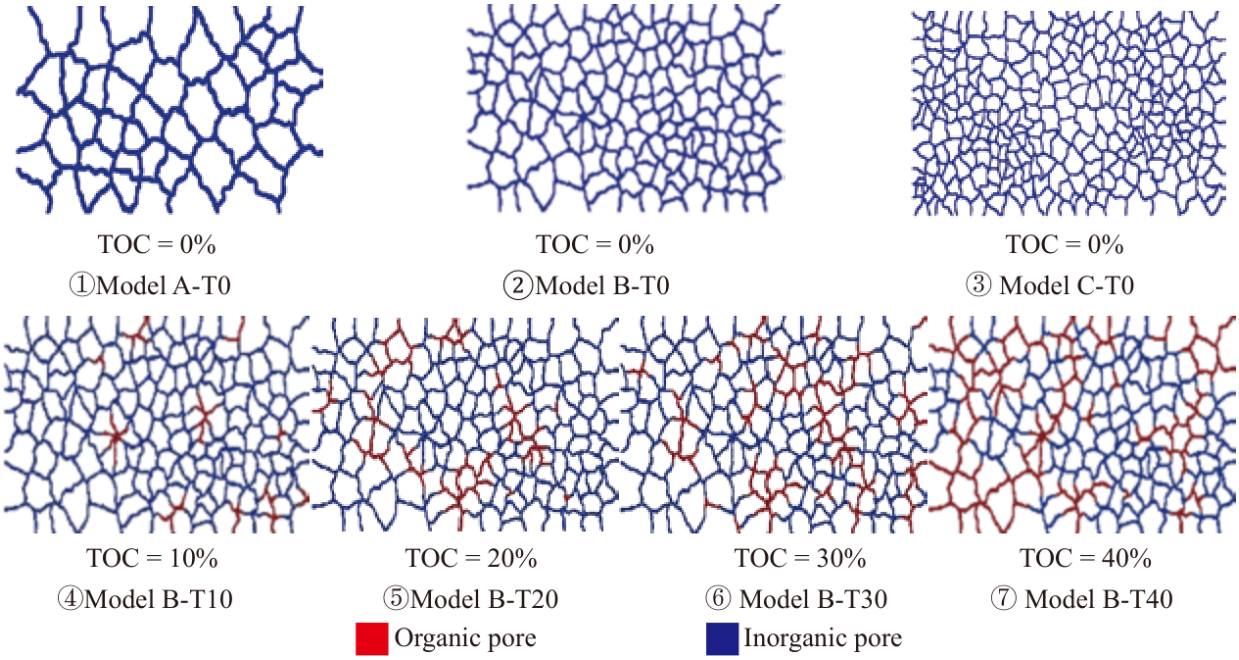


Fig. 2. Porous media models with different TOC contents (Fracture areas are hidden).

havior. The pore radii of the constructed models mainly range from 5 to 30 nm, which corresponds to the pore-size interval where nanoscale confinement has been reported to strongly influence hydrocarbon diffusion. Previous studies have shown that both organic and inorganic pores are widely distributed within this pore size range (Loucks et al., 2009; Chen et al., 2025). Accordingly, based on previously constructed T-shaped models, a prescribed proportion of pores was randomly assigned as organic pores, while the remaining pores were designated as inorganic pores. A random assignment strategy was adopted to approximate the heterogeneous distribution of pore mineral types within shale reservoirs. The total organic carbon content was represented by the volume fraction of pores assigned as organic pores. In this way, a series of nanoporous media models with different TOC contents were generated, as shown in Fig. 2. By varying only the proportion of organic pores while maintaining the pore geometry unchanged, the influence of mineral type on fluid transport behavior could be systematically isolated and evaluated.

2.2 Fluid properties

To characterize component transport in shale oil, n-octane (C_8H_{18}) was selected as the representative hydrocarbon component. The fluid considered in the pore-scale simulations was treated as a single-phase multicomponent liquid mixture, rather than as pure n-octane. To represent the overall hydrodynamic properties of an octane-dominated shale oil system, an equivalent liquid density of 700 kg/m^3 was adopted for the flow simulations, while a dynamic viscosity of 0.312 mPa·s, corresponding to n-octane, was used as the viscosity parameter. The molecular weight of n-octane is 114 g/mol; the relevant physicochemical data were obtained from the NIST Chemistry WebBook. In the species-transport calculations, n-octane was treated as the representative transported component, and only its transport behavior was explicitly resolved. This treatment enabled examining the effects of nanoscale confinement, pore size and pore-wall properties on component transport while avoiding additional uncertainties associated with multicomponent diffusion.

Because molecular diffusivity under nanoscale confinement depends strongly on pore size and pore wall properties, the n-octane diffusion coefficients used in the pore-scale simulations were obtained from molecular dynamics simulations rather than prescribed as a spatially uniform constant. Quartz and Type I-A kerogen nano-slit models were constructed to represent inorganic and organic nanopores, respectively. The quartz, kerogen and n-octane systems were described using the CLAYFF, CVFF and OPLS-AA force fields, respectively. To maintain consistency with the pore-scale simulations, all MD calculations were performed at 383 K and 30 MPa. Five slit half-widths of 1, 2.5, 5, 10, and 20 nm were considered. The slit half-width was used as the characteristic confinement length and mapped to the equivalent pore radius in the subsequent pore-scale diffusion model.

For each nanoslit system, energy minimization was first performed to remove unfavorable initial atomic configurations, followed by a 3-ns equilibration simulation under the prescribed temperature and pressure values. After equilibrium was reached, an additional 1-ns production trajectory was collected for diffusion analysis. The mean square displacement of n-octane molecules was calculated as:

$$\mathrm{MSD}(t) = \left\langle |\mathbf{r}_i(t) - \mathbf{r}_i(0)|^2 \right\rangle \tag{11}$$

where $\mathbf{r}_i(t)$ and $\mathbf{r}_i(0)$ represent the position vectors of molecule i at time t and the reference time, respectively. The self-diffusion coefficient (D) was obtained from the slope of the long-time linear region of the mean square displacement curve according to the Einstein relation (Einstein, 1905) as:

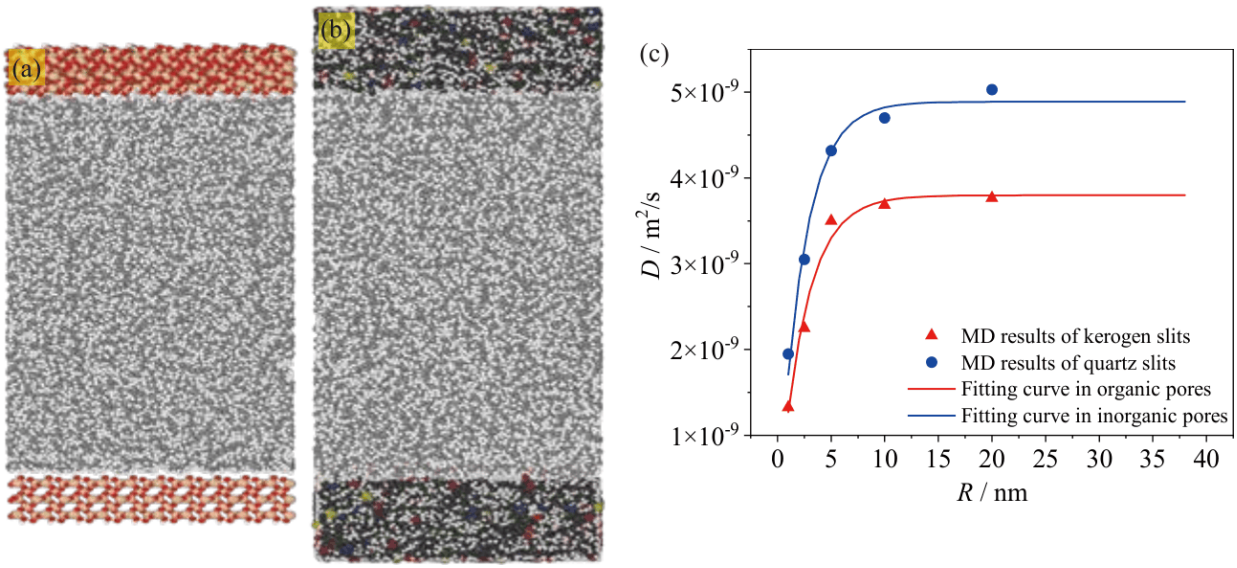


Fig. 3. MD models and pore-radius-dependent diffusion correlations of n-octane: (a) Quartz slit model, (b) kerogen slit model, and (c) diffusion coefficients and fitted curves.

$$D = \frac{1}{6}\frac{\mathrm{d}}{\mathrm{d}t}\mathrm{MSD}(t) \tag{12}$$

As shown in Fig. 3, the MD-derived diffusion coefficients increase rapidly with the pore radius in relatively narrow nanopores and gradually approach a plateau with increasing pore size. This asymptotic behavior cannot be adequately represented by a linear correlation, which would predict an unrealistically continuous increase in diffusivity at large pore sizes. Therefore, the MD data were correlated using a saturation-type exponential function:

$$D(R) = a\left[1-\exp(-bR)\right] \tag{13}$$

where $D(R)$ denotes the self-diffusion coefficient at a pore radius of R; a represents the asymptotic diffusion coefficient at relatively large pore sizes; b characterizes the sensitivity of diffusivity to pore-radius variation; and R is the pore radius. The fitted relationships for inorganic pores (D_i) and organic pores (D_o) were obtained as:

$$\begin{cases} D_{\mathrm{i}} = 4.887774\times10^{-9}\left[1-\exp(-0.42938R)\right] \\ D_{\mathrm{o}} = 3.797115\times10^{-9}\left[1-\exp(-0.40725R)\right] \end{cases} \tag{14}$$

Meanwhile, the coefficients of determination for the two equations were 0.9751 and 0.9778, respectively.

Under identical thermodynamic and pore-size conditions, the diffusion coefficients obtained in Type I-A kerogen nanopores were consistently lower than those in quartz nanopores, indicating a stronger restriction of C_8H_{18} molecular mobility in organic pores. The above MD-derived correlations were subsequently incorporated into the pore-scale transport model, in which the local diffusion coefficient was dynamically assigned according to the local pore radius and pore type. Therefore, the pore-based diffusion coefficient used in this study could be expressed as $D = D(R,\mathrm{Poretype})$ under the fixed thermodynamic condition of 383 K and 30 MPa. The present correlations are specific to these thermodynamic conditions and were not intended as universal pressure- and temperature-independent relationships.

2.3 Mathematical model

In this work, shale oil was regarded as an incompressible fluid, and the mass conservation equations and momentum equations were expressed as:

$$\nabla\cdot\mathbf{u} = 0 \tag{15}$$

$$\rho\left(\frac{\partial\mathbf{u}}{\partial t}+\mathbf{u}\cdot\nabla\mathbf{u}\right) = -\nabla p+\mu\nabla^2\mathbf{u} \tag{16}$$

where $\mathbf{u}$ denotes velocity; μ denotes viscosity; p denotes pressure; ρ denotes density; and t is time.

On the basis of the governing equations for fluid flow, a species mass conservation analysis was further performed to describe the transport behavior of solute components in the fluid. Considering the combined effects of advection and molecular diffusion, species transport is governed by the following convection-diffusion equation:

$$\frac{\partial c_j}{\partial t}+\nabla\cdot(\mathbf{u}c_j) = \nabla\cdot(D_j\nabla C_j) \tag{17}$$

where C_j denotes the concentration of species j; and D_j represents the diffusion coefficient of species j.

The above governing equations were numerically solved using the *interTransportFoam* solver developed on the OpenFOAM platform (Maes and Menke, 2021). This solver is based on the finite volume method, in which the continuity equation, momentum conservation equation, and species transport equation are discretized and solved over the computational domain.

In the original *interTransportFoam* implementation adopted in this study, the diffusion coefficient of each species in a given phase is prescribed as a constant. Consequently, the original formulation cannot explicitly represent nanoscale-confined diffusion in heterogeneous porous media, where molecular diffusivity varies with local pore size and pore-wall

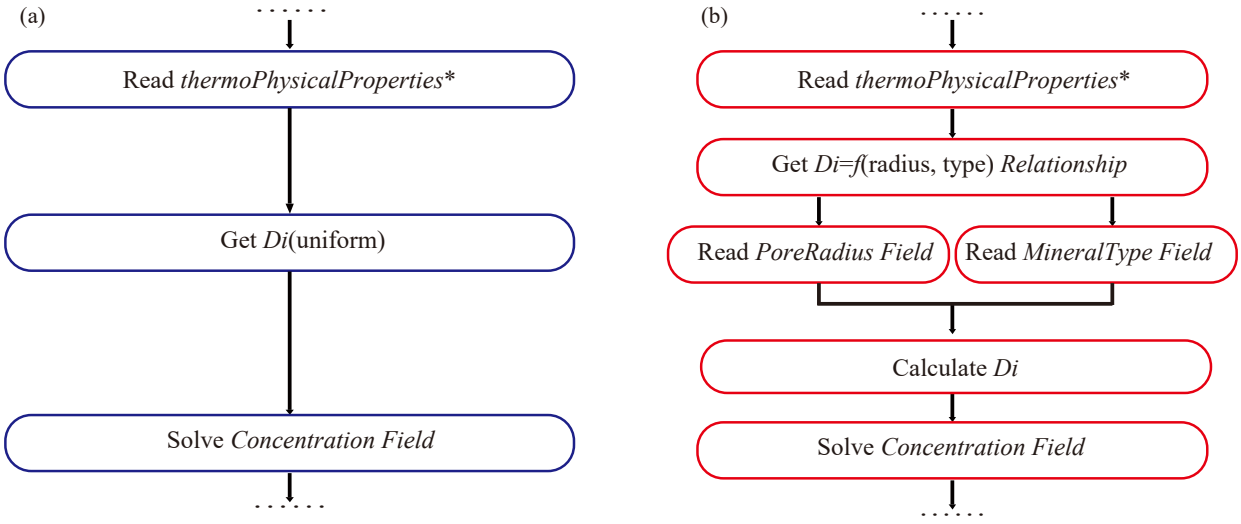


Fig. 4. Solver workflows: (a) Original *interTransportFoam* and (b) modified *interTransportFoam* with the pore-based diffusion model.

properties. To address this limitation, the diffusion-coefficient formulation was modified in the present study, so that the local diffusivity varies according to both pore radius and pore type.

The spatially varying diffusion coefficient was incorporated into the species-transport equation in conservative divergence form:

$$\frac{\partial c_j}{\partial t} + \nabla \cdot (\mathbf{u} c_j) = \nabla \cdot (D_j(x) \nabla C_j) \tag{18}$$

where $D_j(x)$ represents the local diffusion coefficient determined by the pore radius and pore type. In the modified OpenFOAM solver, the diffusion term was discretized using the implicit finite-volume operator fvm :: laplacian(D, C_j), with D defined as a face-based diffusion-coefficient field. The Laplacian term was discretized using the Gauss linear corrected scheme, and the corrected surface-normal gradient treatment was employed to account for mesh non-orthogonality.

Because the finite-volume formulation evaluates a single diffusive flux at each internal face, this flux contributes to the two adjacent control volumes with equal magnitude and opposite signs. Therefore, local species-mass conservation is preserved even when the diffusion coefficient differs between neighboring pore regions because of variations in pore radius or pore type. No additional interfacial source term or concentration-jump condition was imposed between different pore regions; instead, the effect of spatially heterogeneous diffusivity was incorporated directly through the face diffusive flux in the conservative discretization.

Compared with the original implementation, the modified model additionally requires the spatial fields *MineralType* and *PoreRadius*, together with the diffusion coefficient-pore radius correlations corresponding to different pore types. These inputs were used to construct the spatially varying diffusion-coefficient field employed in the species-transport calculation.

During each simulation step, the modified diffusion-coefficient model first reads the user-defined diffusion coefficient-pore radius relationships for different pore mineral types from the configuration file. For each computational cell, the local pore mineral type was obtained from the *MineralType* field to determine the corresponding diffusion coefficient-pore radius relationship. The local pore radius was then extracted from the *PoreRadius* field, and the local diffusion coefficient was calculated according to the selected relationship. The calculated diffusion coefficient was subsequently assigned to the corresponding computational cell and employed in the discretization and solution of the species transport equation.

With these modifications, the solver dynamically updates the local diffusion coefficient throughout the computational domain according to the spatial distributions of pore radius and pore mineral type, thereby incorporating the pore-based diffusion model into the species transport equation. The overall solution procedure of the modified solver is illustrated in Fig. 4.

To verify the implementation and numerical accuracy of the developed solver, a one-dimensional transient diffusion problem in a straight nanotube was selected as the benchmark case. Under the assumptions of an ideal fluid, initially uniform concentration, constant concentrations at both ends, no flow, and one-dimensional molecular diffusion, the governing equations could be reduced to a one-dimensional transient diffusion equation. Since the fluid remains stationary throughout the simulation, convective transport vanishes and molecular diffusion becomes the only transport mechanism. The corresponding analytical solution can be expressed as the sum of a steady-state term and a transient term (Li et al., 2015):

$$C(x,t) = C_1 + \frac{C_r - C_1}{L} x + \sum_{n=1}^{\infty} B_n \sin\left(\frac{n\pi x}{L}\right) \exp\left[-D\left(\frac{n\pi}{L}\right)^2 t\right] \tag{19}$$

$$B_n = \begin{cases} \dfrac{2(C_r - C_1)}{n\pi}, & \text{for even } n \\ \dfrac{2\left[2(C_{ini} - C_1) - (C_r - C_1)\right]}{n\pi}, & \text{for odd } n \end{cases} \tag{20}$$

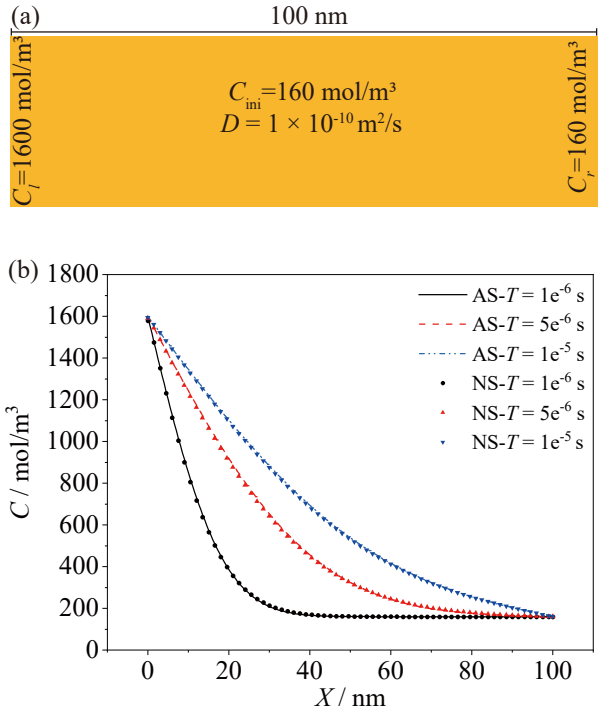


Fig. 5. Verification of the one-dimensional diffusion model: (a) Computational domain and (b) comparison between the analytical (AS) and numerical (NS) concentration profiles.

Table 2. Simulation parameters for implementation verification of the pore-based diffusion coefficient model.

Variable	Value
Inlet-outlet pressure difference (Pa)	10
Test fluid viscosity (mPa·s)	0.312
Test fluid density (kg/m^3)	700
Test fluid diffusion coefficient (10^{-9} m^2/s)	$D_i = 10[1-\exp(-0.05R)]$ $D_o = 5[1-\exp(-0.05R)]$
Initial concentration in fracture region (mol/m^3)	557.7
Initial concentration in pore region (mol/m^3)	5,577

where C denotes the concentration; L denotes the length of the model; x denotes the spatial coordinate; B_n represents the amplitude coefficient of the nth mode; n denotes the order of the Fourier series; C_{ini} denotes the initial concentration; C_l denotes the concentration at the left boundary; and C_r denotes the concentration at the right boundary.

The model domain length was 100 nm, with an initial concentration of 160 mol/m^3. The concentration at the left boundary was 1,600 mol/m^3, while that at the right boundary was 160 mol/m^3. The diffusion coefficient was set to 1×10^{-10} m^2/s. The model setup and the comparison between the simulation results and the analytical solution are shown in Fig. 5. The numerical results agree well with the analytical solution over the entire simulation period, confirming the correctness of the solver implementation and its capability to accurately simulate transient diffusion processes.

To verify the numerical implementation of the pore-based diffusion coefficient model in the modified solver, a cross-shaped heterogeneous test domain was constructed, as shown in Fig. 6(a). The domain contains regions with different pore types and pore radii, enabling the procedures for reading the *MineralType* and *PoreRadius* fields, evaluating the corresponding local diffusion coefficients, and incorporating the resulting diffusion-coefficient field into the species-transport equation to be tested simultaneously. The simulation parameters used for the verification are listed in Table 2. The diffusion-coefficient correlations adopted in this verification case were intentionally prescribed test functions and are independent of the MD-derived correlations used in the subsequent physical simulations.

Two calculations were performed using identical geometry, initial conditions, boundary conditions, and fluid properties. In the first case, the diffusion coefficients corresponding to each pore region were directly prescribed according to the test correlations listed in Table 2. In the second case, only the *MineralType* and *PoreRadius* fields were supplied, and the modified solver dynamically evaluated the local diffusion coefficient using the same correlations. Therefore, the directly prescribed case provides a numerical reference for assessing whether the newly implemented pore-based diffusion procedure reproduces the intended diffusion-coefficient field and species-transport solution.

To verify the numerical implementation of the pore-based diffusion model, the results obtained using dynamically evaluated diffusion coefficients were compared with those from a prescribed-coefficient case under identical computational conditions. The concentration profiles from the two cases are presented in Fig. 6(b). The two results are nearly coincident over the entire sampling line, including regions adjacent to the interfaces between different pore types and pore radii. This agreement confirms that the modified solver correctly reads the pore-property fields, evaluates the local diffusion coefficient according to the prescribed $D(R)$ relationships, and incorporates the spatially varying diffusion coefficient into the species-transport equation without introducing implementation errors. It should be emphasized that this comparison serves as an implementation verification rather than a physical validation of the diffusion-coefficient correlations themselves. The physical basis of the diffusion-coefficient model was established separately through the MD simulations described in Section 2.2.

2.4 Simulation settings

Based on the shale multi-mineral nanoporous models constructed in Section 2.1, the equivalent fluid properties described in Section 2.2, and the modified numerical solver presented in Section 2.3, a series of pore-scale simulations were performed to investigate the transport behavior of shale oil components under nanoscale confinement. The porous-me-

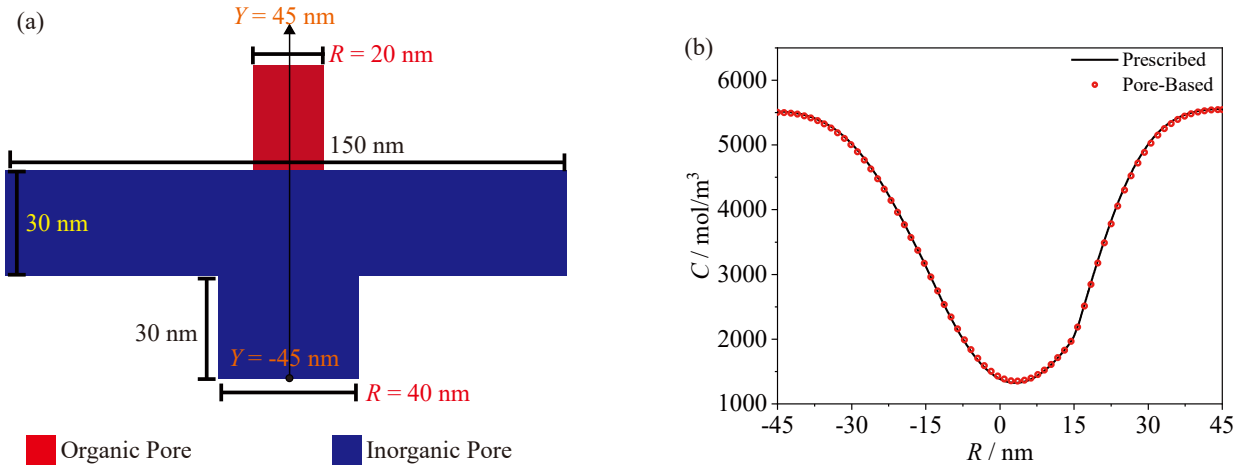


Fig. 6. Verification of the pore-based diffusion model: (a) Verification geometry and (b) concentration profiles obtained using prescribed and dynamically evaluated diffusion coefficients.

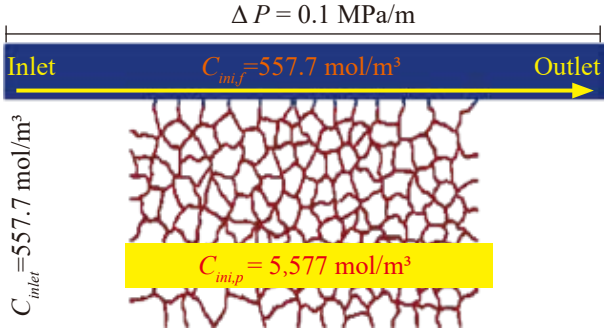


Fig. 7. Schematic illustration of selected simulation setups.

dium models were discretized using the *snappyHexMesh* utility in OpenFOAM, and the species-transport equation was solved using the modified *interTransportFoam* solver incorporating the proposed pore-based diffusion-coefficient model. The fluid system was treated as the single-phase multicomponent liquid described in Section 2.2, with an equivalent density of 700 kg/m^3 and a dynamic viscosity of 0.312 mPa·s. N-octane (C_8H_{18}) was used as the representative transported component. The diffusion-coefficient correlations correspond to the fixed thermodynamic condition of 383 K and 30 MPa.

As illustrated in Fig. 7, the two ends of the fracture were defined as the inlet and outlet boundaries. The porous medium was connected to the external domain only through the fracture and had no direct connection with either the inlet or the outlet boundaries. Pressure boundary conditions were applied at both inlet and outlet, with a pressure gradient (ΔP) = 0.1 MPa/m. To simulate the diffusion of shale oil components from the porous matrix toward the fracture, the inlet concentration (C_{inlet}) and the initial concentration in the fracture region ($C_{ini,f}$) were both set to 557.7 mol/m^3, while the initial concentration in the porous medium region ($C_{ini,p}$) was set to 5577 mol/m^3. These values represent the molar concentration of C_8H_{18} as a component of the same single-phase liquid mixture, rather than the molar density of pure n-octane in different phase states. To represent a C_8H_{18}-depleted fracture liquid and to establish the initial matrix-fracture concentration difference, the fracture concentration was prescribed as 10% of the matrix concentration. No gas phase, vapor-liquid equilibrium, evaporation, or phase transition was considered in the present model. Therefore, the simulated process represents C_8H_{18} transport within a single liquid phase rather than the diffusion of liquid n-octane into a gaseous n-octane phase. Zero-gradient boundary conditions were imposed for velocity at both inlet and outlet. The simulation results were output every 1×10^{-5} s, and the total simulation time was 5×10^{-4} s.

On the basis of the above simulation setup, the numerical experiments summarized in Table 3 were conducted to systematically investigate the effects of the pore-based diffusion model, pore radius, and TOC on the diffusion behavior of shale oil components in shale nanoporous media. By varying one factor and keeping the others unchanged, the individual influence of each parameter on the diffusion process could be isolated and quantitatively evaluated.

3. Result and discussion

3.1 Effect of the pore-based diffusion model

To evaluate the influence of nanoscale confinement on component transport, the results obtained using the pore-based diffusion model were compared with those of the corresponding uniform-diffusion reference case. In the pore-based model, the local diffusion coefficient was dynamically determined according to the pore radius and pore type, whereas a spatially uniform diffusion coefficient was employed in the reference case.

To quantify the influence of the pore-based diffusion model on matrix-fracture mass transfer, the temporal evolution of the average n-octane concentration in the porous-medium region was analyzed, as shown in Fig. 8(a). It can be seen that the average concentration obtained with the pore-based diffusion ($C_{p\text{-}d}$) model remains consistently higher than that of the uniform-diffusion (C_{uni}) case, indicating slower depletion of n-octane from the nanoporous matrix. As shown in Fig. 8(b), the concentration difference between the two cases increases

Table 3. Nano-porous media models selected for different research targets.

Research targets	Model used	Additional operation
Effect of pore-based diffusion model	Model B-T0-Uni-PoreRadius Model B-T20	In Section 3.1, Model B-T0 is modified by uniformly assigning the poreRadius field to 61.875 nm, generating Model B-T0-Uni-PoreRadius
Effect of Pore Radius	Model A-T0; Model B-T0; Model C-T0	/
Effect of TOC	Model B-T0; Model B-T10; Model B-T20 Model B-T30; Model B-T40 Model B-T20-Uni-PoreRadius	In Section 3.3, Model B-T20 is modified by uniformly assigning the poreRadius field to 9.328 nm, generating Model B-T20-Uni-PoreRadius

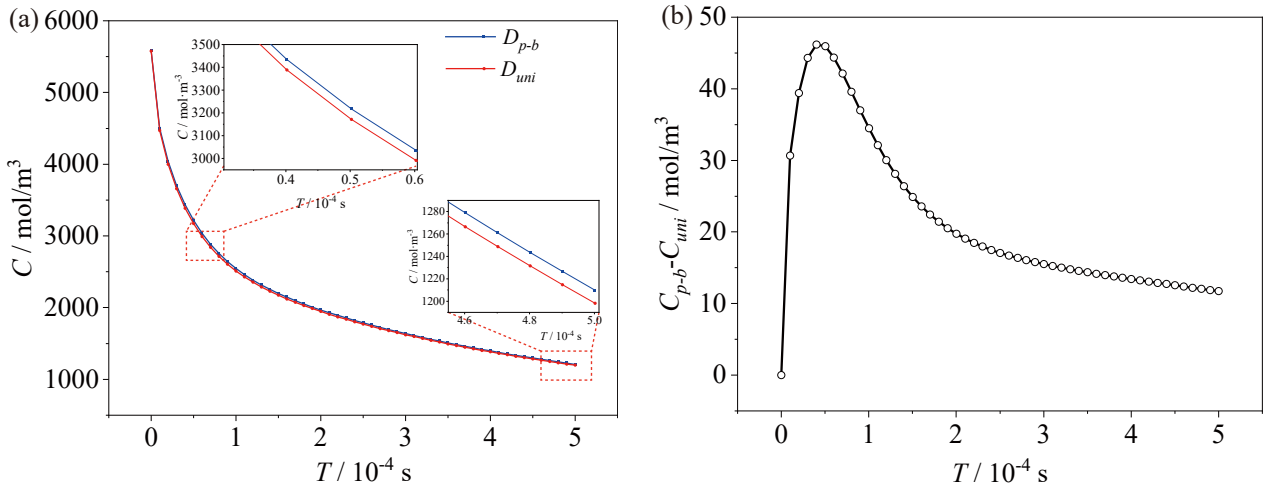


Fig. 8. Influence of the pore-based diffusion model on n-octane transport: (a) Temporal evolution of average concentration and (b) concentration difference.

rapidly during the early stage of transport, reaches a maximum of approximately 46.2 mol/m^3 at time $T \approx 4.0 \times 10^{-5}$ s, and subsequently decreases as the matrix-fracture concentration gradient weakens. At $T = 5.0 \times 10^{-4}$ s, the average concentrations are approximately 1,209.9 and 1,198.2 mol/m^3 for the pore-based and uniform-diffusion cases, respectively. These results indicate that nanoscale confinement primarily affects the transient matrix-fracture mass-transfer rate and leads to a greater retention of n-octane within the nanoporous matrix.

In addition to the average concentration in the porous media region, the coefficient of variation of concentration (ξ) was further employed to characterize the uniformity of the concentration distribution, and its calculation is given as (Pélabon et al., 2020):

$$\xi = \sqrt{\frac{\frac{1}{n-1}\sum_{i=1}^{n}(c_i - \bar{c})^2}{\frac{1}{n}\sum_{i=1}^{n} c_i}} \tag{21}$$

where ξ represents the coefficient of variation of concentration; c_i represents the n-octane concentration at the i^{th} grid point in the porous media region; $\bar{c}$ denotes the average n-octane concentration in the porous media region; and n represents the total number of grid points in the porous media region. Although the ξ decreased continuously as the concentration field evolved, it remained higher in the pore-based diffusion case than in the uniform-diffusion case. The maximum relative difference in ξ was approximately 5.83% at $T \approx 7.0 \times 10^{-5}$ s. At the end of the simulation, the ξ values were 0.06134 and 0.05920 for the pore-based and uniform-diffusion cases, respectively, corresponding to a relative difference of approximately 3.61%. This indicates that the spatial variation in diffusivity caused by differences in pore radius and pore type produces a moderately more heterogeneous concentration distribution, even though the overall concentration fields gradually approach similar late-stage distributions. That is, smaller and organic pores exhibit relatively lower diffusivities and therefore retain n-octane for longer periods than larger or inorganic pores.

The relative importance of advective and diffusive transport was further evaluated using the Péclet number according to Eq. (1). Using a representative diffusion coefficient of 3.5×10^{-9} m^2/s, the maximum velocity in the fracture region (approximately 5.6×10^{-7} m/s) and its characteristic length (approximately 1.7 μm) yielded Pe $\approx 2.7 \times 10^{-4}$. More importantly, the maximum velocity within the porous-medium

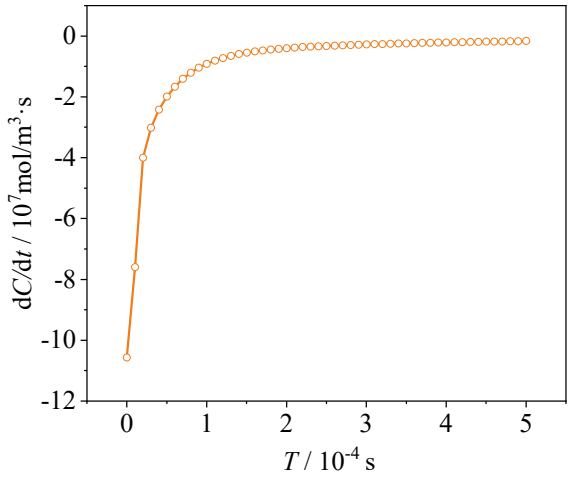


Fig. 9. Temporal evolution of rate of change of the average n-octane concentration in the porous-medium region.

region was only approximately 3.2×10^{-9} m/s. Using a characteristic matrix length of 1.0 μm yielded Pe $\approx 9.1 \times 10^{-7}$. Both values are far below unity, particularly within the nanoporous matrix, demonstrating that component transport under the present conditions was strongly diffusion dominated. Therefore, the differences observed between the two diffusion models are primarily associated with the modification of molecular diffusivity by nanoscale confinement rather than with advective transport.

To further evaluate the temporal evolution of the mass-transfer process, the rate of change in the average n-octane concentration in the porous-medium region was calculated by $\mathrm{d}C/\mathrm{d}t$, where C represents the volume-averaged n-octane concentration in the porous-medium region. As shown in Fig. 9, $\mathrm{d}C/\mathrm{d}t$ is strongly negative during the initial stage because of the large matrix-fracture concentration gradient. Its magnitude decreases rapidly with time and gradually approaches zero as the concentration gradient weakens. By $T = 5 \times 10^{-4}$ s, the concentration-change rate has decreased substantially compared with its initial value, indicating that the system has entered a late-stage quasi-steady depletion regime. Although complete concentration equilibrium has not yet been reached, the small concentration change rate indicates that further concentration variation becomes limited over the investigated time scale.

Overall, the results demonstrate that nanoscale confinement primarily suppresses the transient diffusive transfer of n-octane from the nanoporous matrix to the fracture. The spatially varying diffusion coefficient not only slows the overall depletion of the matrix but also produces a moderately more heterogeneous concentration distribution, as reflected by the higher ξ. As the concentration gradient decreases, the difference between the pore-based and uniform-diffusion cases gradually diminishes and the concentration-change rate approaches zero.

3.2 Effect of pore radius

The influence of pore radius on component diffusion was investigated using Models A, B and C, which have similar porosities but different average pore radii. All pores were assigned as inorganic pores to minimize the influence of pore-type differences.

To examine how pore size affects the local propagation of the concentration front near the fracture, the spatial evolution of n-octane concentration was analyzed. Fig. 10 illustrates the local concentration evolution near the fracture. An isoconcentration contour of $C = 2{,}000$ mol/m^3 was used to trace the concentration front. This value was selected because the concentration in pores near the fracture decreases rapidly from the initial value of 5,577 mol/m^3, and the 2,000 mol/m^3 contour provides a clear indicator of front propagation under the present simulation conditions. It should be emphasized that this contour was used only as a visualization criterion and does not represent a physical phase boundary. The concentration front propagates faster in larger pores and is increasingly retarded with the pore radius decreasing, consistent with the pore-radius-dependent diffusion coefficient established in Section 2.2.

To further quantify the influence of pore radius on matrix-fracture transport, the average n-octane concentration was compared among models with different pore sizes. Fig. 11(a) further shows that the average n-octane concentration decreases more slowly as the average pore radius decreases, indicating stronger component retention within smaller-pore structures. Taking Model A–with the largest average pore radius–as the reference (C_A), Fig. 11(b) reveals that the concentration difference increases from Model B to Model C (C_i). These results demonstrate that decreasing pore radius reduces the overall diffusion capacity of the porous medium and suppresses matrix-fracture component transport.

3.3 Effect of TOC

In Section 3.3, the *PoreRadius* field in the porous-medium region of *Model B-T20* was uniformly assigned a value of 9.328 nm, corresponding to the average pore radius of Model B, thereby constructing *Model B-T20-Uni-PoreRadius*. By eliminating the influence of pore radius, the observed differences in diffusion behavior can be attributed solely to variations in the pore mineral type.

To evaluate the influence of pore type on local diffusion behavior, the concentration evolution in representative organic and inorganic pores near the fracture was compared. Fig. 12 presents the local concentration evolution in representative organic and inorganic pores near the fracture. Similar to Section 3.2, the $C = 2{,}000$ mol/m^3 isoconcentration contour was used to trace the propagation of the concentration front. This contour serves only as a visualization criterion and does not represent a physical phase boundary. Under the same pore-radius condition, the concentration front propagates more slowly in organic pores than in inorganic pores, indicating stronger confinement of n-octane transport in organic nanopores. This behavior is consistent with the MD-derived diffusion correlations in Section 2.2, which give lower n-octane diffusivities in Type I-A kerogen pores than in quartz pores under identical pore-size and thermodynamic conditions.

The local difference between organic and inorganic pores is further reflected in the overall transport behavior at different

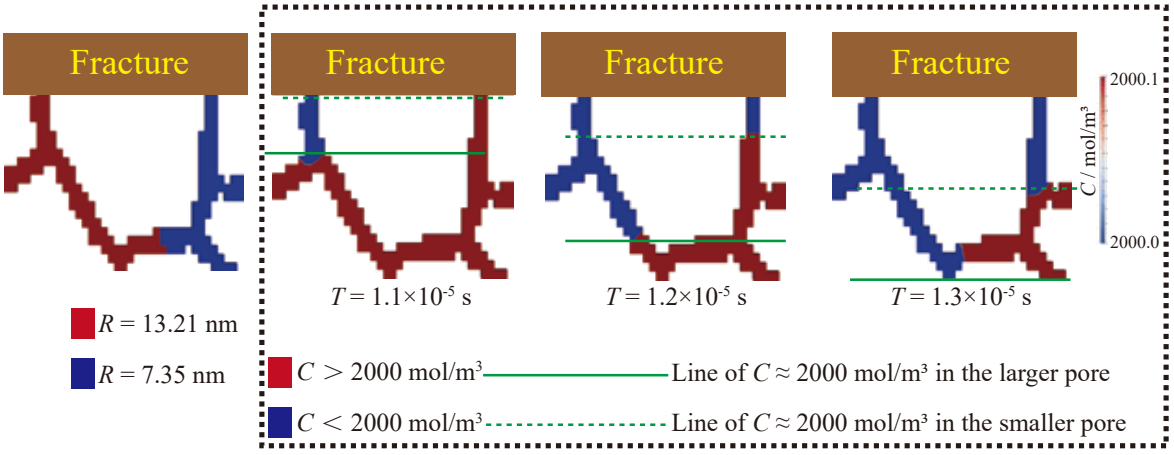


Fig. 10. Local concentration evolution near the fracture for models with different pore radii: Distribution of (a) pore radius and (b) concentration.

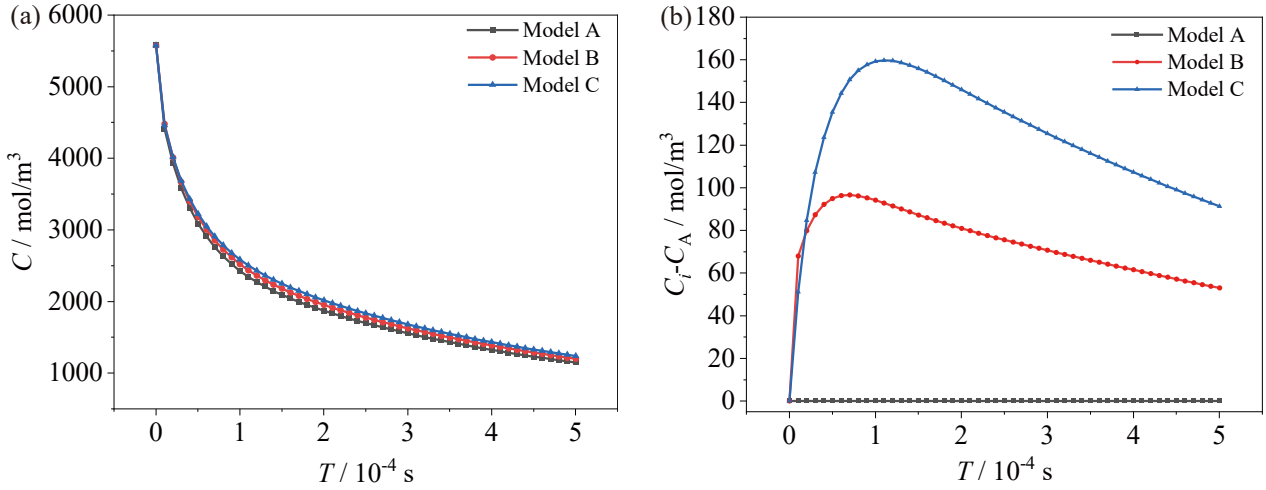


Fig. 11. Effect of pore radius on n-octane transport: (a) Temporal evolution of average concentration in different models and (b) concentration difference between different models.

TOC values. As shown in Fig. 13(a), the average n-octane concentration in the porous-medium region increases systematically with increasing TOC, indicating progressively slower depletion of the matrix. Taking B0 as the reference (C_{T0}), Fig. 13(b) further shows that the concentration difference generally increases with TOC (C_j). At the end of the simulation, the average concentrations for B0, B10, B20, B30, and B40 are approximately 1,200.4, 1,203.2, 1,209.9, 1,210.5, and 1,223.4 mol/m^3, respectively. The increasing proportion of organic pores therefore reduces the effective diffusion capacity of the porous medium and enhances component retention within the matrix.

Overall, these results indicate that pore-wall properties and TOC influence matrix-fracture component transport via modifying the spatial distribution of local diffusivity. Increasing TOC elevates the proportion of low-diffusivity organic pores and consequently suppresses the release of n-octane from the nanoporous matrix.

4. Conclusions

In this study, a pore-based diffusion model was developed to incorporate molecular-scale confinement effects into pore-scale simulations of shale oil component transport. Using MD-derived relationships for n-octane in quartz and Type I-A kerogen nanopores at 383 K and 30 MPa, the local diffusion coefficient was formulated as a function of pore radius and pore type. The modified OpenFOAM solver was verified against an analytical diffusion solution, and the numerical implementation of the pore-based diffusion procedure was independently verified.

The results showed that nanoscale confinement suppresses matrix-fracture component transport by reducing local molecular diffusivity. Compared with the uniform-diffusion reference case, the pore-based model produced a maximum average-concentration difference of approximately 46.2 mol/m^3 and approximately 1.83% greater excess residual component retention at 5×10^{-4} s. The maximum relative difference in the concentration coefficient of variation was approximately

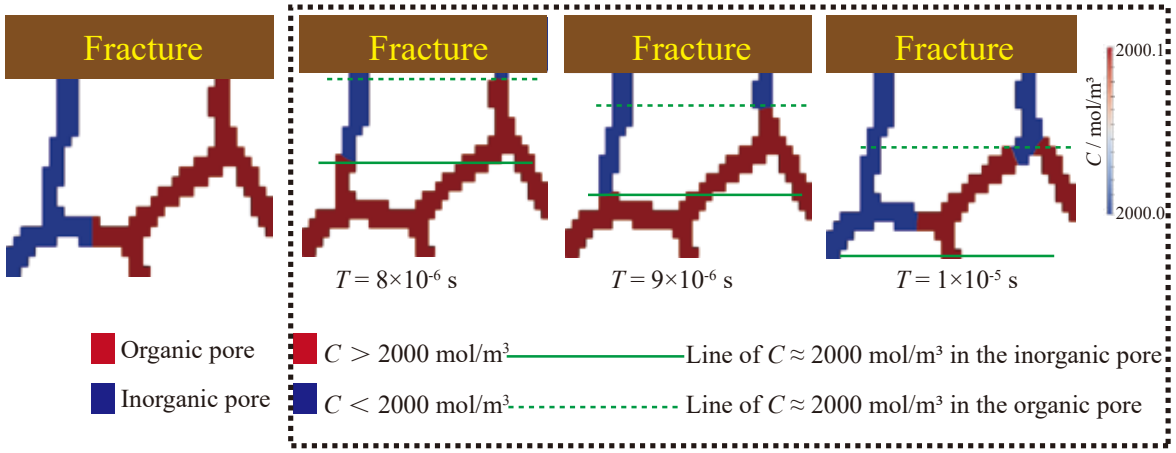


Fig. 12. Local concentration evolution in representative organic and inorganic pores near the fracture: Distribution of (a) pore type and (b) concentration.

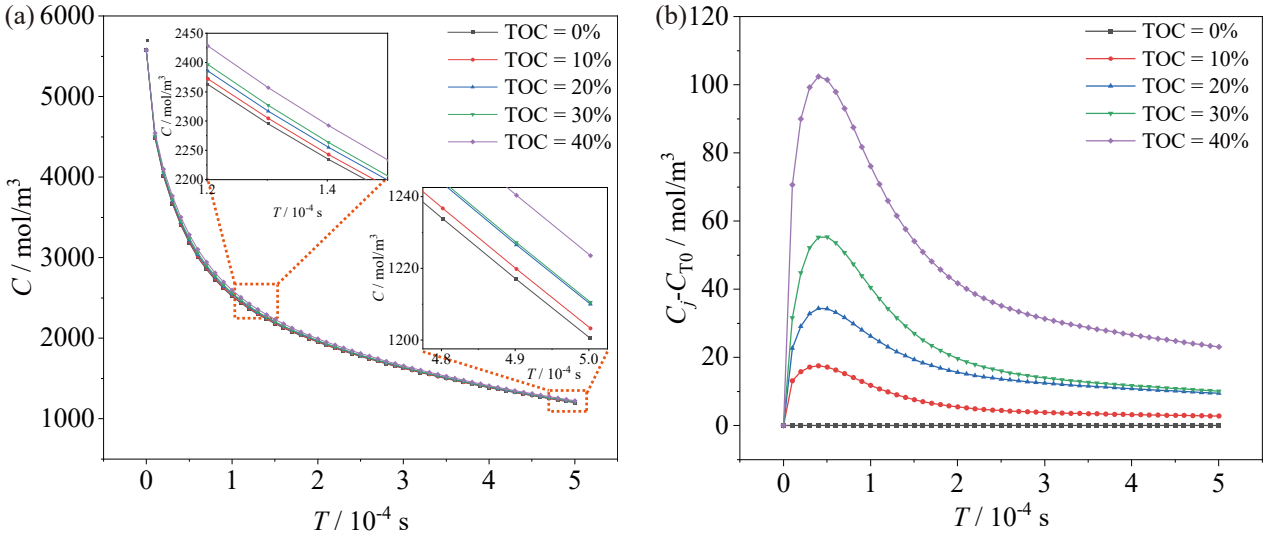


Fig. 13. Effect of TOC on n-octane transport: (a) Temporal evolution of average concentration in different TOC models and (b) concentration difference between different TOC models.

5.83%, indicating moderately enhanced spatial heterogeneity. Péclet-number analysis further confirmed that transport within the nanoporous matrix was strongly dominated by diffusion. Decreasing pore radius reduced the overall diffusion capacity, while organic pores exhibited lower n-octane diffusivities than inorganic pores under identical conditions. Consequently, increasing TOC from 0% to 40% raised the final excess residual component retention by approximately 3.58%.

The proposed model considers a single-phase multicomponent liquid system with n-octane as the representative transported component. Therein, compressibility, multicomponent cross-diffusion, and phase behavior are not explicitly considered, and the present diffusion correlations are specific to 383 K and 30 MPa. Future work should extend the framework to more complex thermodynamic and multicomponent conditions. Overall, the proposed model provides a practical molecular-to-pore-scale framework for representing spatially heterogeneous diffusivity and evaluating shale oil component retention under nanoscale confinement.

Acknowledgements

We would like to express our appreciation for the financial support of the following institutions: The National Natural Science Foundation of China (Nos. U23A20595 and 52288101), the Shandong Provincial Natural Science Foundation (No. ZR2024ZD17), and the Fundamental Research Funds for the Central Universities (No. 23CX10004A). The authors also thank the Xi'an Supercomputing Center for the support during the development.

Conflicts of interest

The authors declare no competing interest.

Open Access This article is distributed under the terms and conditions of the Creative Commons Attribution (CC BY-NC-ND) license, which permits unrestricted use, distribution, and reproduction in any medium, provided the

original work is properly cited.

References

Bao, J., Du, J., Zhan, S., et al. A molecular perspective on the microscopic mechanisms of CO_2 injection and water films in fluid transport and enhanced oil recovery. Advances in Geo-Energy Research, 2025, 16(3): 288-292.

Bousige, C., Ghimbeu, C. M., Vix-Guterl, C., et al. Realistic molecular model of kerogen's nanostructure. Nature Materials, 2016, 15(5): 576-582.

Cai, J., Jiao, X., Wang, H., et al. Multiphase fluid-rock interactions and flow behaviors in shale nanopores: A comprehensive review. Earth-Science Reviews, 2024a, 257: 104884.

Cai, J., Qin, X., Xia, X., et al. Numerical modeling of multiphase flow in porous media considering micro- and nanoscale effects: A comprehensive review. Gas Science and Engineering, 2024b, 131: 205441.

Chen, S., Li, X., Zhu, G., et al. Classification, controlling factors, and multi-scale characterization techniques in shale reservoir pores: A comprehensive review. Gas Science and Engineering, 2025, 140: 205662.

Cui, F., Jin, X., Liu, H., et al. Molecular modeling on gulong shale oil and wettability of reservoir matrix. Capillarity, 2022, 5(4): 65-74.

Dong, X., Xu, W., Liu, R., et al. Insights into adsorption and diffusion behavior of shale oil in slit nanopores: A molecular dynamics simulation study. Journal of Molecular Liquids, 2022, 359: 119322.

Du, Q., Faber, V., Gunzburger, M. Centroidal voronoi tessellations: Applications and algorithms. SIAM Review, 1999, 41(4): 637-676.

Duan, L., Sun, H., Zhang, L., et al. A method for pore-scale simulation of single-phase shale oil flow based on three-dimensional digital cores with hybrid mineral phases. Physics of Fluids, 2022, 34(6): 062010.

Einstein, A. On the motion of small particles suspended in liquids at rest required by the molecular-kinetic theory of heat. Annals of Physics, 1905, 322(8): 549-560. (in German)

Fei, J., Wang, M., Li, J., et al. Molecular dynamics simulation of adsorption and absorption behavior of shale oil in realistic kerogen slits. Energy & Fuels, 2023, 37(5): 3654-3671.

Feng, Q., Xing, X., Wang, S., et al. CO_2 diffusion in shale oil based on molecular simulation and pore network model. Fuel, 2024, 359: 130332.

Fu, E., He, W. The development and utilization of shale oil and gas resources in china and economic analysis of energy security under the background of global energy crisis. Journal of Petroleum Exploration and Production Technology, 2024, 14(8): 2315-2341.

Huysmans, M., Dassargues, A. Review of the use of péclet numbers to determine the relative importance of advection and diffusion in low permeability environments. Hydrogeology Journal, 2005, 13(5): 895-904.

Jia, L., Gao, Z., Li, Z., et al. Micro-migration of shale oil and its interaction mechanism with inorganic minerals. Advances in Geo-Energy Research, 2026, 21(2): 185-197.

Ji, L., Lin, M., Cao, G., et al. A core-scale reconstructing method for shale. Scientific Reports, 2019, 9(1): 4364.

Li, Z., Yazdani, A., Tartakovsky, A., et al. Transport dissipative particle dynamics model for mesoscopic advection-diffusion-reaction problems. The Journal of Chemical Physics, 2015, 143(1): 014101.

Liu, J., Xiao, D., Li, J., et al. Enhanced oil recovery via CO_2 flooding in tight reservoirs: A pore-scale analysis. Advances in Geo-Energy Research, 2025, 17(2): 162-175.

Loucks, R. G., Reed, R. M., Ruppel, S. C., et al. Morphology, genesis, and distribution of nanometer-scale pores in siliceous mudstones of the mississippian barnett shale. Journal of Sedimentary Research, 2009, 79(12): 848-861.

Luo, C., Cheng, J., Ba, J., et al. A modeling-inversion methodology for source rocks based on clay-kerogen lamination and pore geometry. Petroleum Science, 2025, 22(11): 4462-4491.

Lv, C., Yang, Y., Zhang, Q., et al. The effect of solid-liquid interfacial interactions on shale oil flow in the micro-nano scale porous media. SPE Journal, 2026, 31(07): 4814-4832.

Maes, J., Menke, H. P. Geochemfoam: Direct modelling of multiphase reactive transport in real pore geometries with equilibrium reactions. Transport in Porous Media, 2021, 139(2): 271-299.

Maurer, C. R., Rensheng, Q., Raghavan, V. A linear time algorithm for computing exact euclidean distance transforms of binary images in arbitrary dimensions. IEEE Transactions on Pattern Analysis and Machine Intelligence, 2003, 25(2): 265-270.

Pélabon, C., Hilde, C. H., Einum, S., et al. On the use of the coefficient of variation to quantify and compare trait variation. Evolution Letters, 2020, 4(3): 180-188.

Sang, Q., Guo, X., Dong, M. Occurrence mechanism of shale oil in laminated shale reservoirs: A review. Petroleum Science, 2026, 23(4): 1773-1803.

Song, W., Liu, F., Li, Y., et al. Pore scale modeling of fluid transport in complex reservoirs: Multi-scale digital rock construction, flow experiments and simulation methods. Capillarity, 2024, 11(3): 81-88.

Song, W., Yao, J., Zhang, K. Study on gas adsorption and transport behavior in shale organic nanopore. Chinese Journal of Theoretical and Applied Mechanics, 2021, 53(8): 2179-2192.

Tran, S., Yassin, M. R., Eghbali, S., et al. Quantifying oil-recovery mechanisms during natural-gas huff 'n' puff experiments on ultratight core plugs. SPE Journal, 2021, 26(1): 498-514.

Voronoi, G. New applications of continuous parameters to the theory of quadratic forms. Second memoir: Research on primitive parallelohedra. Journal for Pure and Applied Mathematics, 1908, 1908(134): 198-287. (in French)

Wang, H., Wang, X., Jin, X., et al. Molecular dynamics

simulation of diffusion of shale oils in montmorillonite. The Journal of Physical Chemistry C, 2016, 120(16): 8986-8991.

Wang, H., Xia, X., Zhao, F., et al. Pore-scale study on CO_2 miscible displacement of shale oil considering competitive adsorption. Langmuir, 2025a, 41(48): 32637-32649.

Wang, L., Zhang, Y., Zou, R., et al. Applications of molecular dynamics simulation in studying shale oil reservoirs at the nanoscale: Advances, challenges and perspectives. Petroleum Science, 2025b, 22(1): 234-254.

Wang, S., Feng, Q., Zha, M., et al. Supercritical methane diffusion in shale nanopores: Effects of pressure, mineral types, and moisture content. Energy & Fuels, 2018, 32(1): 169-180.

Wang, S., Liang, Y., Feng, Q., et al. Sticky layers affect oil transport through the nanopores of realistic shale kerogen. Fuel, 2022, 310: 122480.

Wu, M., Xiao, F., Johnson-Paben, R. M., et al. Single- and two-phase flow in microfluidic porous media analogs based on voronoi tessellation. Lab on a Chip, 2012, 12(2): 253-261.

Xiang, M., Xu, S., Wen, Y., et al. Influence of tectonic preservation conditions on the nanopore structure of shale reservoir: A case study of wufeng-longmaxi formation shale in western hubei area, south china. Petroleum Science, 2024, 21(4): 2203-2217.

Xiao, F., Yin, X. Geometry models of porous media based on voronoi tessellations and their porosity-permeability relations. Computers & Mathematics with Applications, 2016, 72(2): 328-348.

Xu, S., Yang, Z., Wu, S., et al. Fractal analysis of pore structure differences between shale and sandstone based on the nitrogen adsorption method. Natural Resources Research, 2022, 31(3): 1759-1773.

Xu, S., Zhao, T., Cui, X., et al. Organic-inorganic interactions of clay minerals and organic matter: Action mechanism and analysis techniques. Advances in Geo-Energy Research, 2024, 14(3): 161-164.

Xu, Y., Lun, Z., Pan, Z., et al. Occurrence space and state of shale oil: A review. Journal of Petroleum Science and Engineering, 2022, 211: 110183.

Xue, C., Ji, D., Cheng, D., et al. Adsorption behaviors of different components of shale oil in quartz slits studied by molecular simulation. ACS Omega, 2022, 7(45): 41189-41200.

Yang, Y., Liu, F., Zhang, Q., et al. Recent advances in multiscale digital rock reconstruction, flow simulation, and experiments during shale gas production. Energy & Fuels, 2023, 37(4): 2475-2497.

Yang, Y., Wang, K., Zhang, L., et al. Pore-scale simulation of shale oil flow based on pore network model. Fuel, 2019, 251: 683-692.

Zhan, S., Bao, J., Wang, X., et al. A comparative study of shale oil transport behavior in graphene and kerogen nanopores with various roughness via molecular dynamics simulations. Chemical Engineering Journal, 2024, 498: 155173.

Zhang, C., Zhao, S., Zhao, J., et al. Three-dimensional voronoi analysis of realistic grain packing: An xct assisted set voronoi tessellation framework. Powder Technology, 2021, 379: 251-264.

Zhang, T., Hu, Q., Tian, Q., et al. Small angle neutron scattering studies of shale oil occurrence status at nanopores. Advances in Geo-Energy Research, 2024, 11(3): 230-240.

Zhang, Q., Yang, Y., Zhang, L., et al. Remobilization mechanism of microscopic residual oil in sandstone reservoirs at the high water-cut stage. Chinese Journal of Theoretical and Applied Mechanics, 2025a, 57(12): 2814-2824. (in Chinese)

Zhang, W., Feng, Q., Wang, S., et al. Oil diffusion in shale nanopores: Insight of molecular dynamics simulation. Journal of Molecular Liquids, 2019, 290: 111183.

Zhang, X., Shao, S., Ye, Q., et al. Microscopic insights into shale oil adsorption and diffusion characteristics in kerogen nanopores: Roles of pore size and water content. Journal of Molecular Liquids, 2025b, 438: 128699.

Zhao, J., Kang, Q., Yao, J., et al. The effect of wettability heterogeneity on relative permeability of two-phase flow in porous media: A lattice boltzmann study. Water Resources Research, 2018, 54(2): 1295-1311.

Zhao, W., Liu, S., Bian, C., et al. “Component flow” of shale oil and its significance for sweet spot evaluation in the permian lucaogou formation, jimsaer sag, junggar basin, china. Petroleum Exploration and Development, 2026, 53(3): 612-624.

Zhong, Y., Zhou, J., Xian, X., et al. Diffusion of pure CH_4, CO_2, and their mixtures in shale under various pressures and temperatures. Energy & Fuels, 2025, 39(36): 17361-17370.